Earthquake Science
地震学报英文版 ISSN 1674-4519 CN 11-5695/P

Rapid source inversions of the 2023 SE Türkiye earthquakes with teleseismic and strong-motion data

Chenyu Xu, Yong Zhang, Sibo Hua, Xu Zhang, Lisheng Xu, Yuntai Chen, Tuncay Taymaz

Citation: Xu CY, Zhang Y, Hua SB, Zhang X, Xu LS, Chen YT, Taymaz T (2023). Rapid source inversions of the 2023 SE T ü rkiye earthquakes with teleseismic and strong-motion data. *Earthquake Science*, **36**(4): 316–327, doi: 10.1016/j.eqs.2023.05.004

View online: http://www.equsci.org.cn/article/doi/10.1016/j.eqs.2023.05.004

Earthquake Science 36 (2023) 316–327

Contents lists available at ScienceDirect

Earthquake Science

Journal homepage: https://www.keaipublishing.com/en/journals/earthquake-science/

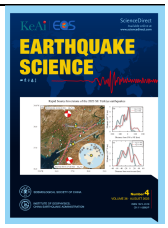

Special Focus/Rapid Communication

Rapid source inversions of the 2023 SE Türkiye earthquakes with teleseismic and strong-motion data

Chenyu Xu[1], Yong Zhang[1,✉], Sibo Hua[1], Xu Zhang[2], Lisheng Xu[2], Yuntai Chen[1,2] and Tuncay Taymaz[3]

[1] *School of Earth and Space Sciences*, *Peking University*, *Beijing* 100871, *China*
[2] *Institute of Geophysics*, *China Earthquake Administration*, *Beijing* 100081, *China*
[3] *Istanbul Technical University*, *The Faculty of Mines*, *Department of Geophysical Engineering*, 34467 *Sariyer*, *Istanbul*, *Türkiye*

Key points:

- We performed fast inversions of rupture process for the two 2023 SE Türkiye earthquake doublet with teleseismic data and strong-motion data.
- Both teleseismic and strong-motion rupture models suggest that the first M_W7.8 earthquake was larger in magnitude, fault length, and duration, but smaller in peak value of moment rate.
- The consistency between teleseismic and strong-motion models suggests a good prospect of applying the strong-motion inversion method in future emergency responses.

A B S T R A C T

We conducted rapid inversions of rupture process for the 2023 earthquake doublet occurred in SE Türkiye, the first with a magnitude of M_W7.8 and the second with a magnitude of M_W7.6, using teleseismic and strong-motion data. The teleseismic rupture models of the both events were obtained approximately 88 and 55 minutes after their occurrences, respectively. The rupture models indicated that the first event was an asymmetric bilateral event with ruptures mainly propagating to the northeast, while the second one was a unilateral event with ruptures propagating to the west. This information could be useful in locating the meizoseismal areas. Compared with teleseismic models, the strong-motion models showed relatively higher resolution. A noticeable difference was found for the M_W7.6 earthquake, for which the strong-motion models shows a bilateral event, rather than a unilateral event, but the dominant rupture direction is still westward. Nevertheless, all strong-motion models are consistent with the teleseismic models in terms of magnitudes, durations, and dominant rupture directions. This suggests that both teleseismic and strong-motion data can be used for fast determination of major source characteristics. In contrast, the strong-motion data would be preferable in future emergency responses since they are recorded earlier and have a better resolution ability on the source ruptures.

Keywords: the 2023 earthquake doublet in SE Türkiye; fast source inversion; teleseismic inversion; strong-motion inversion

✉ **Corresponding author.** Zhang Y, email: zhang-yong@pku.edu.cn

Article history:
Received 14 March 2023
Received in revised form 5 April 2023
Accepted 9 April 2023
Available online 21 April 2023

https://doi.org/10.1016/j.eqs.2023.05.004

Citation: Xu CY, Zhang Y, Hua SB, Zhang X, Xu LS, Chen YT and Taymaz T (2023). Rapid source inversions of the 2023 SE Türkiye earthquakes with teleseismic and strong-motion data. Earthq Sci **36**(4): 316–327, doi: 10.1016/j.eqs.2023.05.004.

1. Introduction

Fast source inversion provides timely and detailed source information for earthquake emergency responses and disaster assessments. In a long time, it was performed with the global teleseismic data (Zhang Y et al., 2012a; Taymaz et al., 1991; 2021) which can be easily obtained from the Incorporated Research Institutions for Seismology (IRIS) data center. Some institutes, such as United States Geological Survey (USGS) (Hayes, 2017; Goldberg et al., 2022), have determined and released teleseismic models for significant large earthquakes. In China, the rupture models were found critical to estimate the meizoseismal areas during the 2008 Wenchuan earthquake. After that, several research groups in China Earthquake Administration and Chinese Academy of Sciences have conducted fast inversion of rupture process with teleseismic data (e.g., Zhang Y et al., 2012a). After more than 10 years' efforts, the rupture models can be determined several hours after an earthquake, providing important source information for responses of many disastrous earthquakes, such as the 2010 M_W6.9 Yushu earthquake (Zhang Y et al., 2010), the 2013 M_W6.6 Lushan earthquake (Wang WM et al., 2013; Zhang Y et al., 2013), and the 2014 M_W6.1 Ludian earthquake (Zhang Y et al., 2014a).

As the teleseismic stations are thousands of kilometers away from the epicenter, the inverted models commonly show relatively low resolution. In addition, since the seismic waves cost at least several minutes to reach the teleseismic stations, the inversion cannot be initiated immediately after an earthquake. In real cases, the teleseismic data of an earthquake from the IRIS data center

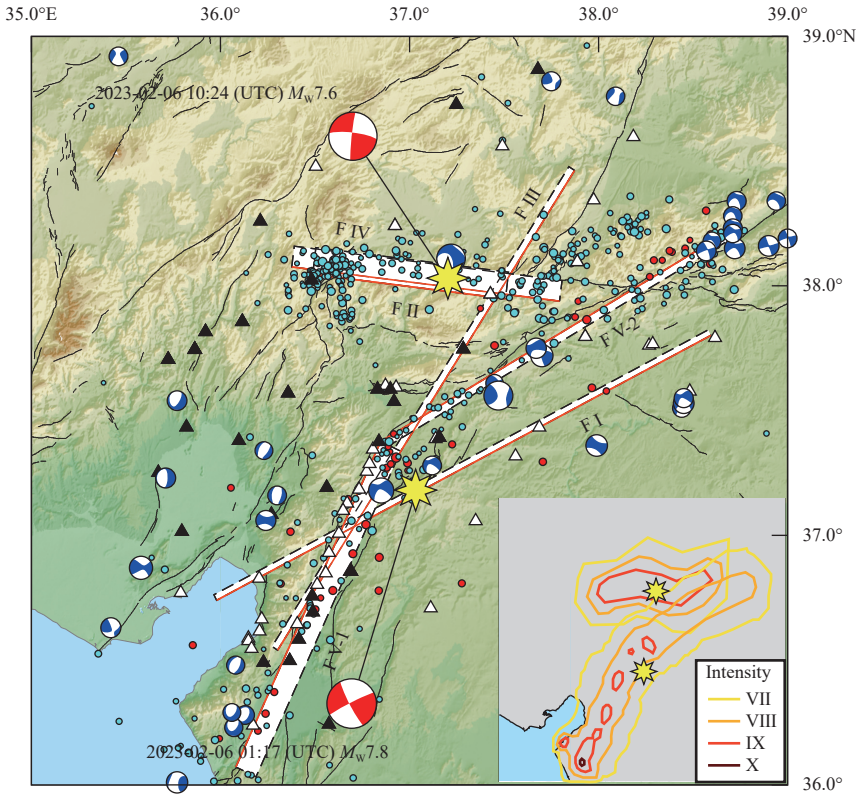

Figure 1. Map view of the epicentral area of the 2023 SE Türkiye earthquakes. Yellow stars represent the epicenters of the two earthquakes given by the USGS. Red and cyan circles show the aftershocks before and after the M_W7.6 earthquake, respectively. F I and II are teleseismic fault models, and F III, IV, V-1, and V-2 are strong-motion fault models. Triangles represent the strong-motion stations while black ones are used in inversions after screening. Beach balls in blue color denote previous earthquakes reported by the Global Centroid Moment Tensor (GCMT) (Ekström et al., 2012). Black lines denote the active fault lines in Türkiye (Emre et al., 2013, 2018). The intensity maps of the two events are given by the Bogazici University (Hancılar et al., 2023) and the USGS Shakemap, respectively.

are usually ready for download about 30 minutes after the occurrence, causing limited efficiency of the rapid report.

In contrast to teleseismic data, near-field strong-motion waveform data are recorded much earlier and are more suitable for fast responses (Zhang Y et al., 2014b). So far, the strong-motion data are rarely applied to fast source inversions even in regions with good observation conditions. This is largely due to the absence of a centralized data center, such as IRIS, to collect and release strong-motion records all over the world, making it difficult to obtain and process the data quickly. However, with the increasing deployment of strong-motion stations worldwide, it is important to study and discuss their potential applicability to fast source inversions.

On 6 February 2023, two large earthquakes with moment magnitudes M_W7.8 and M_W7.6 successively struck the SE Türkiye and the NW of Syria, causing 50,096 deaths in Türkiye as reported by the Disaster and Emergency Management Authority (AFAD) on 20 March. According to USGS, the M_W7.8 earthquake occurred at 04:17:35 local time (01:17:35 UTC), located at 37.174°N, 37.032°E with a depth of 17.9 km, and the M_W7.6 earthquake occurred at 13:24:49 local time (10:24:49 UTC), located at 38.024°N, 37.203°E with a depth of 17.0 km. Much effort has been made to determine the characteristics of these two seismic events (Chen WK et al., 2023; Erdik et al., 2023; Jiang XY et al., 2023). After the occurrence of the two earthquakes, they are both recorded by Global Seismographic Network (GSN) and the local strong-motion network. In this work, we performed teleseismic and strong-motion inversions for the two major events. By comparing the obtained rupture models, we aim to discuss and explore the potential benefits of using near-field data in future fast source inversions.

2. Teleseismic inversion

We utilized teleseismic data from the IRIS data center and removed the instrument responses from vertical P waves before converting them into displacements. The Green's functions used for inversions were obtained from a database calculated using the QSSP codes (Wang RJ et al., 2017) based on the global AK135 model (Kennett et al., 1995).

We first performed fast moment tensor inversions to determine the fault parameters. The obtained fault parameters of the first event are 243°/86°/7° and 153°/83°/176°, with a moment magnitude M_W7.75 (~M_W7.8), and those of the second one are 277°/70°/−2° and 8°/88°/−160°, with a moment magnitude M_W7.57 (~M_W7.6). The obtained magnitudes are slightly less than M_W7.95 and M_W7.86 estimated from long-period coda waves (Jiang XY et al., 2023), but are close to the results of moment tensor solutions from USGS and Global Centroid Moment Tensor (GCMT).

Using the fault parameters 243°/86°/7° for the M_W7.8 earthquake, and 277°/70°/−2° for the M_W7.6 earthquake, we performed finite-fault inversions by using a linear technique (Zhang Y et al., 2012b), and got the rupture models of the two earthquakes about 88 and 55 minutes after their occurrences (Zhang Y et al., 2023). The obtained models of both earthquakes well explain the observed waveforms (Figures S1–S2). As shown in Figure 2,

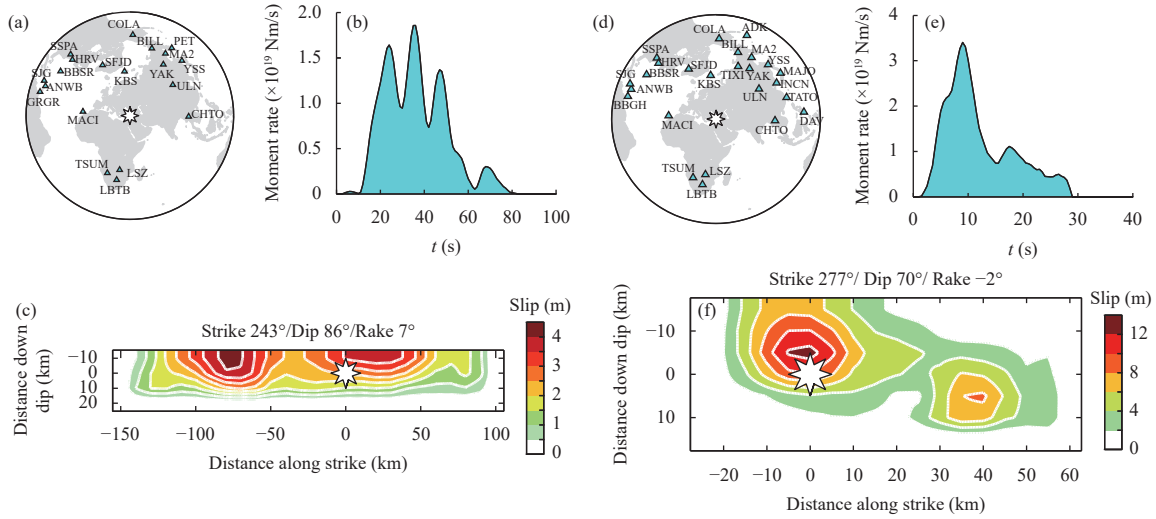

Figure 2. Fast determined teleseismic rupture models of the 6 February 2023 M_W7.8 and M_W7.6 SE Türkiye earthquakes. (a–c) show the distributions of teleseismic stations and epicenter, source time function, and fault slip distribution of the M_W7.8 earthquake. (d–f) are the same to (a–c), but for the M_W7.6 earthquake.

the M_W7.8 earthquake suggests a bilateral rupture event while the M_W7.6 one shows dominant westward unilateral ruptures. It means that the meizoseismal areas of the M_W7.8 earthquake may distribute along the fault, but the highest intensity may appear to the northeast of the epicenter. And for the secondary M_W7.6 earthquake, the source time function has a larger amplitude but a shorter duration, indicating that its energy was fast released in a short time. This may lead to higher intensities than the M_W7.8 earthquake at near-fault distances. Moreover, since the M_W7.6 earthquake is located to the west of the M_W7.8 earthquake fault, its westward ruptures significantly expand the disaster-affected area.

3. Strong-motion inversion

To invert the strong-motion data, we can use an automatic and efficient iterative deconvolution stacking (IDS) method developed by Zhang Y et al. (2014b). Compared with conventional linear or nonlinear method, the IDS method retrieves the rupture model by stacking the sub-fault apparent source time functions at all stations. Because there is no need to solve an inversion problem, the IDS method has a high efficiency and can work automatically (Zhang Y et al., 2014b). In this case, the total time cost of strong-motion inversion is largely dependent on data acquisition. In this work, the strong-motion data are downloaded from the Disaster and Emergency Management Authority (AFAD) of Türkiye approximately one day after the earthquakes. The Green's functions of strong-motion inversions are calculated based on the local CRUST1.0 model (Laske et al., 2012).

The raw acceleration records were corrected for baseline shifts and integrated twice into displacements. To incorporate more data in inversions, we employed the automatic inversion system of Zheng XJ et al. (2020) to screen for individual waveform component, instead of each station. Due to the sensitivity of near-field strong-motion data to the fault position and parameters, simply using the fault models of teleseismic inversions may lead to poor fittings at some near-fault stations. To address this problem, we optimized the fault position and strike through a 2-D grid search, in which all potential strikes, and fault positions varying perpendicular to strike, were tried in inversions. The waveform fittings with the minimum residuals are depicted in Figures S3–S4, while the searched fault models of the M_W7.8 and M_W7.6 earthquakes are presented in Figures 1, 3, and 4 (fault models III and IV). These fault models differ significantly from the teleseismic ones, particularly for the M_W7.8 earthquake, for which the searched strike was only 213°, in contrast to the 243° from teleseismic moment tensor solution. The aftershock distribution suggests that the M_W7.8 earthquake fault is segmented into at least two parts. Since most remaining stations after screening are situated southwest to the epicenter, the searched strike (213°) is primarily associated with the southwest fault segment.

According to the rupture models obtained from strong-motion inversions (depicted in Figure 3), the two earthquakes released scalar moment of 5.33×10^{20} Nm and 3.10×10^{20} Nm, which correspond to moment magnitudes of M_W7.75 and M_W7.59, respectively. These magnitudes are very similar to those calculated from teleseismic

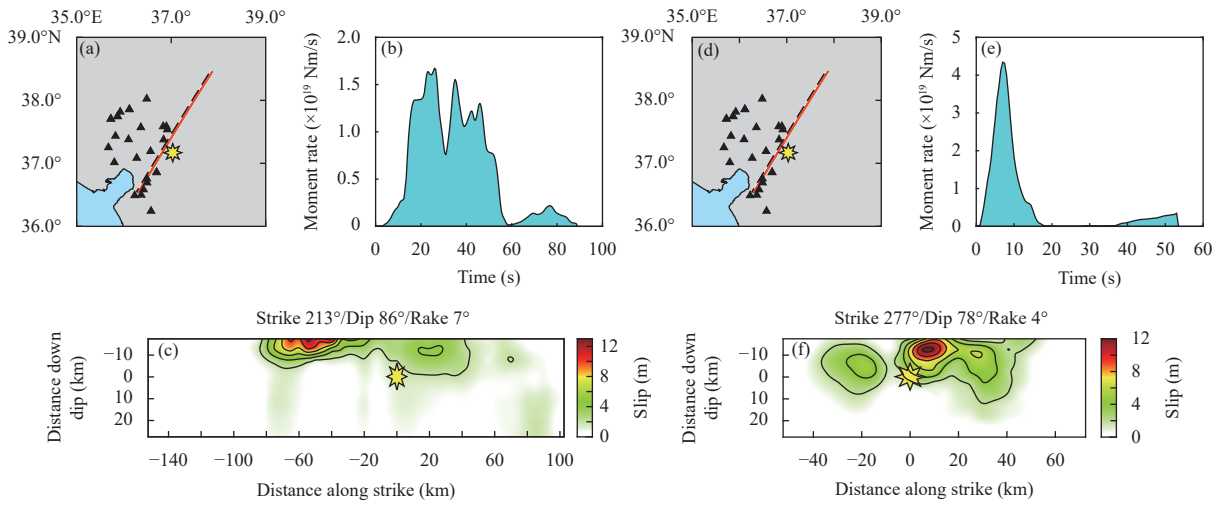

Figure 3. Rupture process results obtained with single-segment fault model of the M_W7.8 and M_W7.6 SE Türkiye earthquake doublet. (a–c) show the distribution of strong-motion stations (triangles), the epicenter (star) and searched fault model, source time function, and slip distribution of the M_W7.8 earthquake. (d–f) are the same to (a–c), but for the M_W7.6 earthquake.

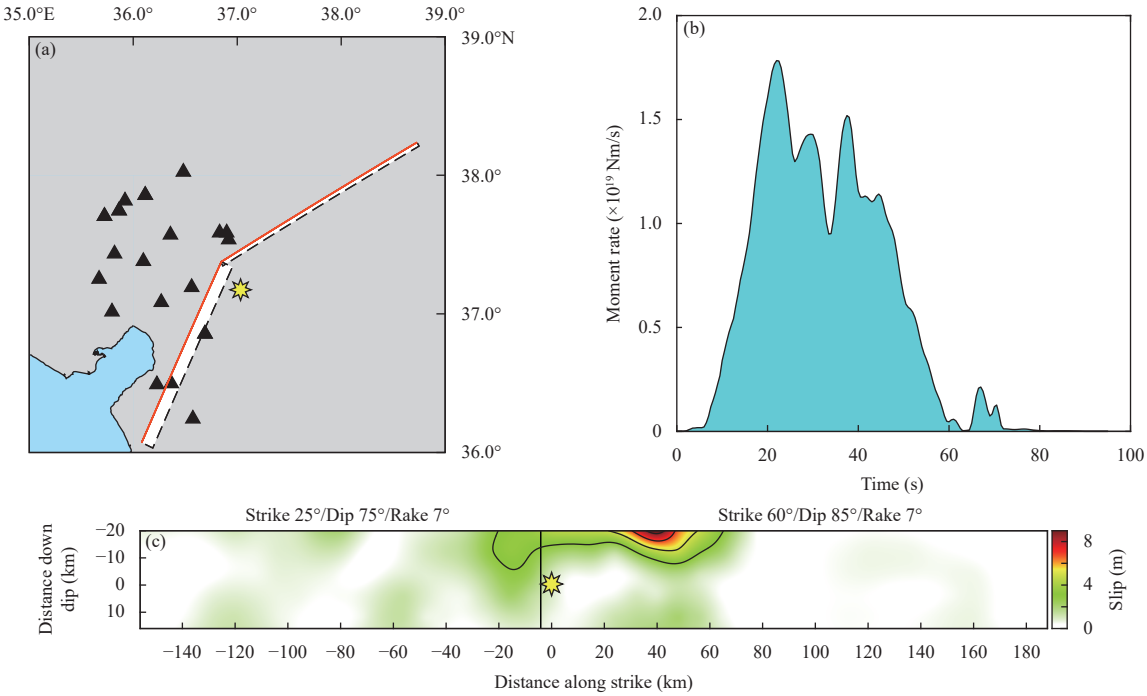

Figure 4. Strong-motion model of the M_W7.8 earthquake estimated based on a two-segment fault. (a–c) show the distribution of strong-motion stations (triangles), the epicenter (star) and two major fault segments given by the USGS, source time function, and fault slip distribution of the M_W7.8 earthquake.

inversions. The M_W7.8 earthquake has a dominant rupture direction to the northeast, which is consistent with the teleseismic model. For the M_W7.6 earthquake, an additional slip patch appears to the east of the epicenter, resulting in a bilateral rupture event. However, both teleseismic and strong-motion models of the M_W7.6 earthquake show a dominant westward rupture direction. Nonetheless, both the teleseismic and strong-motion models agree that the M_W7.8 earthquake is larger in magnitude, fault length, and duration, but smaller in peak value of moment rate. This suggests that the M_W7.6 event had a relatively larger stress drop and a more concentrated energy release history, which may have resulted in higher intensities at the near-fault distances.

4. Discussion and conclusions

Due to the complexity in fault geometry of the M_W7.8 earthquake, it is important to consider alternative fault geometry models when performing a strong-motion inversion. In this study, we utilized a two-segment fault model built by USGS to perform the inversion. The resulted scalar moment and moment magnitude were 5.24×10^{20} Nm are M_W7.75, respectively. The slip distribution was found to be similar to that of the single-fault model (Figures 3 and 4), although the peak slip positions are tens of kilometers apart due to very few stations near the slip concentrated area to the northeast of the epicenter. The misfit values of single-segment and two-segment models are almost identical, but the two-segment model fits more waveform components (Figures S3 and S5).

Unlike strong-motion inversion in which the sub-fault Green′s functions are different in both waveform and time, the sub-fault Green′s functions of teleseismic inversions differ only in time, but are similar in waveform. Therefore, teleseismic inversions mainly rely on the Doppler effects of rupture propagation to determine the relative locations of ruptures compared to the hypocenter, rather than absolute positions. This is why the fault models built using teleseismic moment tensor solutions and searched by strong-motion inversions are distinctly different particularly for the M_W7.8 earthquake. In addition, since the strong-motion data are closer to the source, their inversions show higher resolution ability along both strike and depth (Figure 5). Despite these differences, other rupture features, such as magnitude, duration, dominant rupture direction, and moment distribution, are similar both in teleseismic and strong-motion inversions (Figure 5).

The efficiency of current teleseismic inversion is limited by two factors: (1) data acquisition and (2) manual inversion (Figure 6). For the 2023 SE Türkiye earthquake doublet, it took 30–40 minutes to obtain the data, and the manual inversions required multiple attempts to get

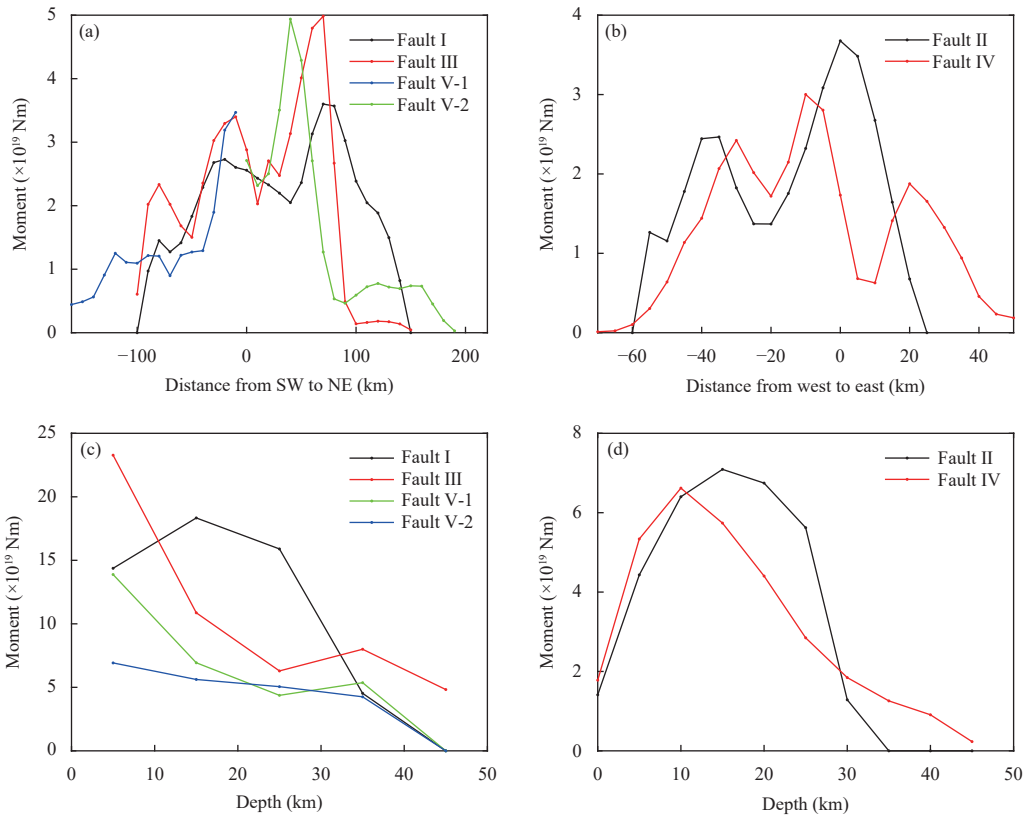

Figure 5. Comparisons of the moment distributions of teleseismic and strong-motion rupture models. (a) Along-strike distribution of the M_W7.8 earthquake. (b) Along-strike distribution of the M_W7.6 earthquake. (c) Along-depth distribution of the M_W7.8 earthquake. (b) Along-depth distribution of the M_W7.6 earthquake.

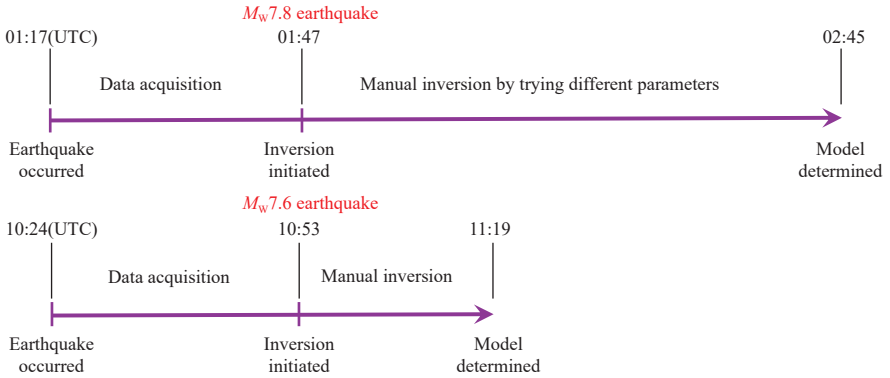

Figure 6. Sketch diagram illustrating the teleseismic inversion flow chart of the 6 February 2023 SE Türkiye earthquake doublet.

reasonable rupture models using a series of inversion parameters. The manual inversions took 58 minutes and 26 minutes for the M_W7.8 and M_W7.6 earthquakes, respectively (Figure 6). For an ideal case of strong-motion inversion, the data would be transmitted in real time and can be ready for inversion within several minutes after the earthquake, and the rupture model can be determined in 1–2 minutes by using the automatic inversion system proposed by Zheng XJ et al. (2020). Considering the total time consuming, including the earthquake location and the determination of the fault parameters, we may determine the rupture model within 10 minutes after an earthquake by inverting strong-motion data.

With the deployment of more regional networks and advancements in communication technology, the near-field waveform data would be available much more conveniently than before. Particularly, the large-scale network of Intensity Rapid Report and Earthquake Early Warning

(IRREEW), which consists of more than 15 000 accelerometers, has been built in Chinese mainland (Peng CY et al., 2019; Li JW et al., 2021). All data of the IRREEW network are transmitted in real time, providing the timeliest waveforms for fast inversions. In the near future, the rupture model could be determined fast and automatically in China, which would much improve our ability in earthquake monitoring and emergency responses.

Data and resources

The teleseismic data used in this study are from the Incorporated Research of Institutions of Seismology (IRIS) data center, and the strong-motion data are provided by the Disaster and Emergency Management Authority (AFAD) of Türkiye. The teleseismic and strong-motion models can be referred to https://pku-geophysics-source.group/index.html.

Acknowledgments

This work is supported by the National Key Research and Development Program of China (2022YFF0800603).

Conflict of interest

Prof. Yong Zhang and Prof. Tuncay Taymaz serve as an editorial board member for *Earthquake Science* and was not involved in the editorial review or the decision-making process for this article. All authors declare that they have no competing interests.

References

Chen WK, Rao G, Kang DJ, Wan ZF and Wang D (2023). Early report of the source characteristics, ground motions, and casualty estimates of the 2023 M_W7.8 and 7.5 Turkey earthquakes. J Earth Sci 1–7. https://doi.org/10.1007/s12583-023-1316-6.

Ekström G, Nettles M and Dziewoński AM (2012). The global CMT project 2004–2010: Centroid-moment tensors for 13, 017 earthquakes. Phys Earth Planet Inter **200-201**: 1–9 https://doi.org/10.1016/j.pepi.2012.04.002.

Emre Ö, Duman TY, Özalp S, Elmacı H, Olgun Ş and Şaroğlu F (2013). Active fault map of Turkey with an explanatory text 1 : 1, 250, 000 scale. General Directorate of Mineral Research and Exploration, Special publication series 30.

Emre Ö, Duman TY, Özalp S, Şaroğlu F, Olgun Ş, Elmacı H and Çan T (2018). Active fault database of Turkey. Bull Earthq Eng **16**(8): 3 229–3 275 https://doi.org/10.1007/s10518-016-0041-2.

Erdik M, Tümsa MBD, Pınar A, Altunel E and Zülfikar AC (2023). A preliminary report on the February 6, 2023 earthquakes in Türkiye. http://doi.org/10.32858/temblor.297.

Goldberg DE, Koch P, Melgar D, Riquelme S and Yeck WL (2022). Beyond the teleseism: Introducing regional seismic and geodetic data into routine USGS finite-fault modeling. Seismol Res Lett **93**(6): 3 308–3 323 https://doi.org/10.1785/0220220047.

Hancılar U, Şeşetyan K, Çaktı E, Şafak E, Yenihayat N, Malcıoğlu FS, Dönmez K, Tetik T and Süleyman H (2023). Kahramanmaraş-Gaziantep Türkiye *M*7.7 earthquake, 6 February 2023 (04: 17 GMT+03: 00), strong ground motion and building damage estimations preliminary report (v6). http://www.koeri.boun.edu.tr/sismo/2/tr/2023/02./.

Hayes GP (2017). The finite, kinematic rupture properties of great-sized earthquakes since 1990. Earth Planet Sci Lett **468**: 94–100 https://doi.org/10.1016/j.epsl.2017.04.003.

Jiang XY, Song XD, Li T and Wu KX (2023). Special focus/Rapid Communication Moment magnitudes of two large Turkish earthquakes on February 6, 2023 from long-period coda. Earthq Sci **36**(2): 169–174 https://doi.org/10.1016/j.eqs.2023.02.008.

Kennett BLN, Engdahl ER and Buland R (1995). Constraints on seismic velocities in the Earth from traveltimes. Geophys J Int **122**(1): 108–124 https://doi.org/10.1111/j.1365-246X.1995.tb03540.x.

Laske G, Masters G, Ma Z and Pasyanos ME (2012). CRUST1.0: An updated global model of Earth′s crust. In: Geophysical Research Abstracts, EGU, **14**: 743.

Li JW, Böse M, Feng Y and Yang C (2021). Real-time characterization of finite rupture and its implication for earthquake early warning: application of FinDer to existing and planned stations in Southwest China. Front Earth Sci **9**: 699560 https://doi.org/10.3389/feart.2021.699560.

Peng CY, Jiang P, Chen QQ, Ma Q and Yang JS (2019). Performance evaluation of a dense MEMS-based seismic sensor array deployed in the Sichuan-Yunnan border region for earthquake early warning. Micromachines (Basel) **10**(11): 735 https://doi.org/10.3390/mi10110735.

Taymaz T, Eyidoğan H and Jackson J (1991). Source parameters of large earthquakes in the East Anatolian Fault Zone (Turkey). Geophy J Int **106**(3): 537–550 https://doi.org/10.1111/j.1365-246X.1991.tb06328.x.

Taymaz T, Ganas A, Yolsal-Çevikbilen S, Vera F, Eken T, Erman C, Keleş D, Kapetanidis V, Valkaniotis S, Karasante I, Tsironi V, Gaebler P, Melgar D and Öcalan T (2021). Source mechanism and rupture process of the 24 January 2020 M_W6.7 Doğanyol-Sivrice earthquake obtained from seismological waveform analysis and space geodetic observations on the East Anatolian Fault Zone (Turkey). Tectonophysics **804**: 228745 https://doi.org/10.1016/j.tecto.

2021.228745.

Wang RJ, Heimann S, Zhang Y, Wang HS and Dahm T (2017). Complete synthetic seismograms based on a spherical self-gravitating Earth model with an atmosphere-ocean-mantle-core structure. Geophys J Int **210**(3): 1 739–1 764 https://doi.org/10.1093/gji/ggx259.

Wang WM, Hao JL and Yao ZX (2013). Preliminary result for rupture process of Apr. 20, 2013, Lushan Earthquake, Sichuan, China. Chin J Geophy **56**(4): 1 412–1 417 https://doi.org/10.6038/cjg20130436 (in Chinese with English abstract).

Zhang Y, Xu LS and Chen YT (2010). Fast inversion of rupture process of the 14 April 2010 Yushu, Qinghai, earthquake. Earthq Sci **23**(3): 201–204 https://doi.org/10.1007/s11589-010-0715-9.

Zhang Y, Chen YT and Xu LS (2012a). Fast and robust inversion of earthquake source rupture process and its application to earthquake emergency response. Earthq Sci **25**(2): 121–128 https://doi.org/10.1007/s11589-012-0838-2.

Zhang Y, Feng WP, Chen YT, Xu LS, Li ZH and Forrest D (2012b). The 2009 L'Aquila M_W 6.3 earthquake: A new technique to locate the hypocentre in the joint inversion of earthquake rupture process. Geophys J Int **191**(3): 1 417–1 426 https://doi.org/10.1111/j.1365-246X.2012.05694.x.

Zhang Y, Xu LS and Chen YT (2013). Rupture process of the Lushan 4.20 earthquake and preliminary analysis on the disaster-causing mechanism. Chin J Geophys **56**(4): 1 408–1 411 https://doi.org/10.6038/cjg20130435 (in Chinese with English abstract).

Zhang Y, Xu LS, Chen YT and Liu RF (2014a). Rupture process of the 3 August 2014 Ludian, Yunnan, M_W6.1(M_S6.5) earthquake. Chinese J Gepphys **57**(9): 3 052–3 059 https://doi.org/10.6038/cjg20140930 (in Chinese with English abstract).

Zhang Y, Wang RJ, Zschau J, Chen YT, Parolai S and Dahm T (2014b). Automatic imaging of earthquake rupture processes by iterative deconvolution and stacking of high-rate GPS and strong motion seismograms. J Geophys Res:Solid Earth **119**(7): 5 633–5 650 https://doi.org/10.1002/2013JB010469.

Zhang Y, Xu CY, Zhang X, Xu LS and Chen YT(2023). Rupture process of the 2023 Turkey earthquakes. https://pku-geophysic-source.group/index.html. (in Chinese).

Zheng XJ, Zhang Y, Wang RJ, Zhao L, Li WY and Huang QH (2020). Automatic inversions of strong-motion records for finite-fault models of significant earthquakes in and around Japan. J Geophys Res:Solid Earth **125**(9): e2 020JB019 992 https://doi.org/10.1029/2020JB019992.

Supplementary information

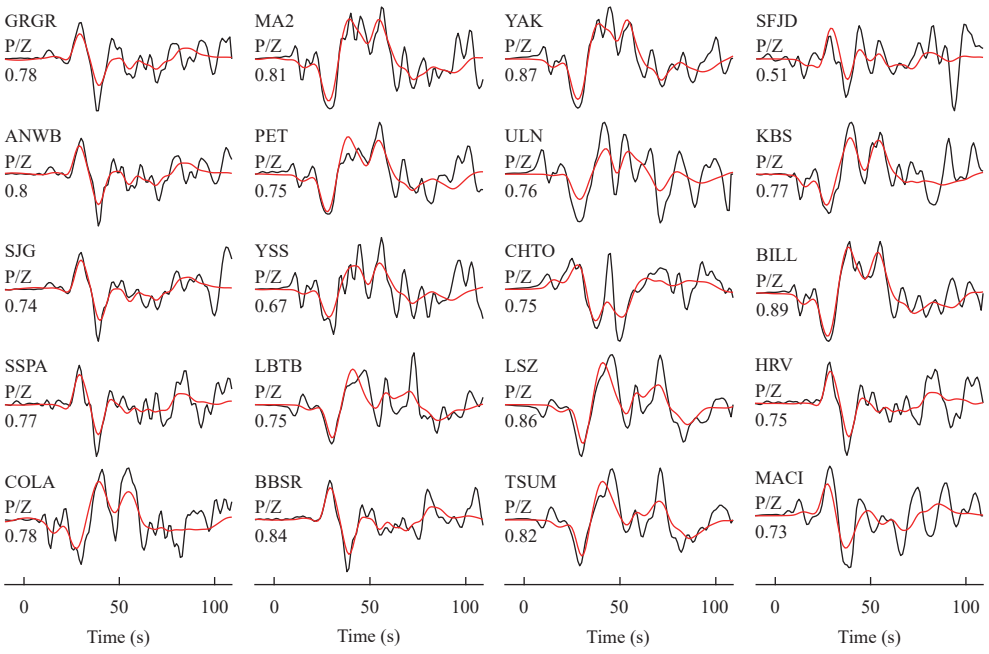

Figure S1. Comparisons between the observed (black) and synthetic P waves (red) for the teleseismic inversion of the M_W7.8 earthquake. The filtering frequency band is 0.01–0.2 Hz. For each station, the station code and correlation coefficient are marked on the top-left and bottom left, respectively.

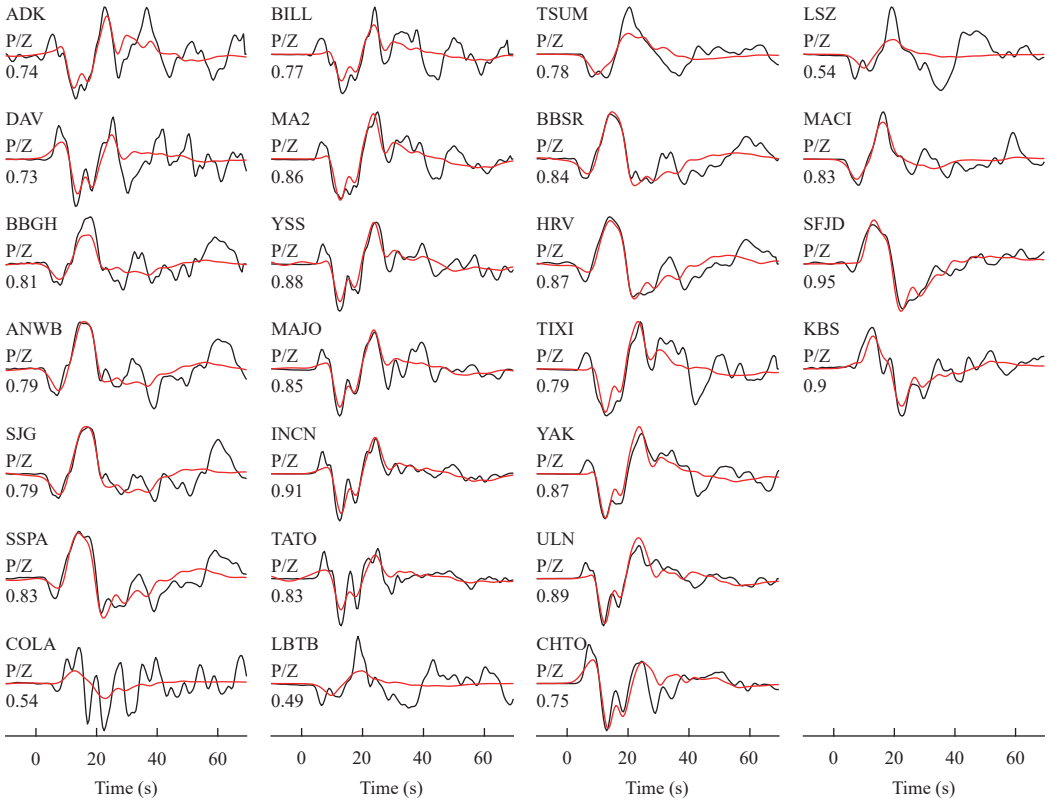

Figure S2. The same as Figure S1 but for the M_W7.6 earthquake. The filtering frequency band is 0.01–0.4 Hz.

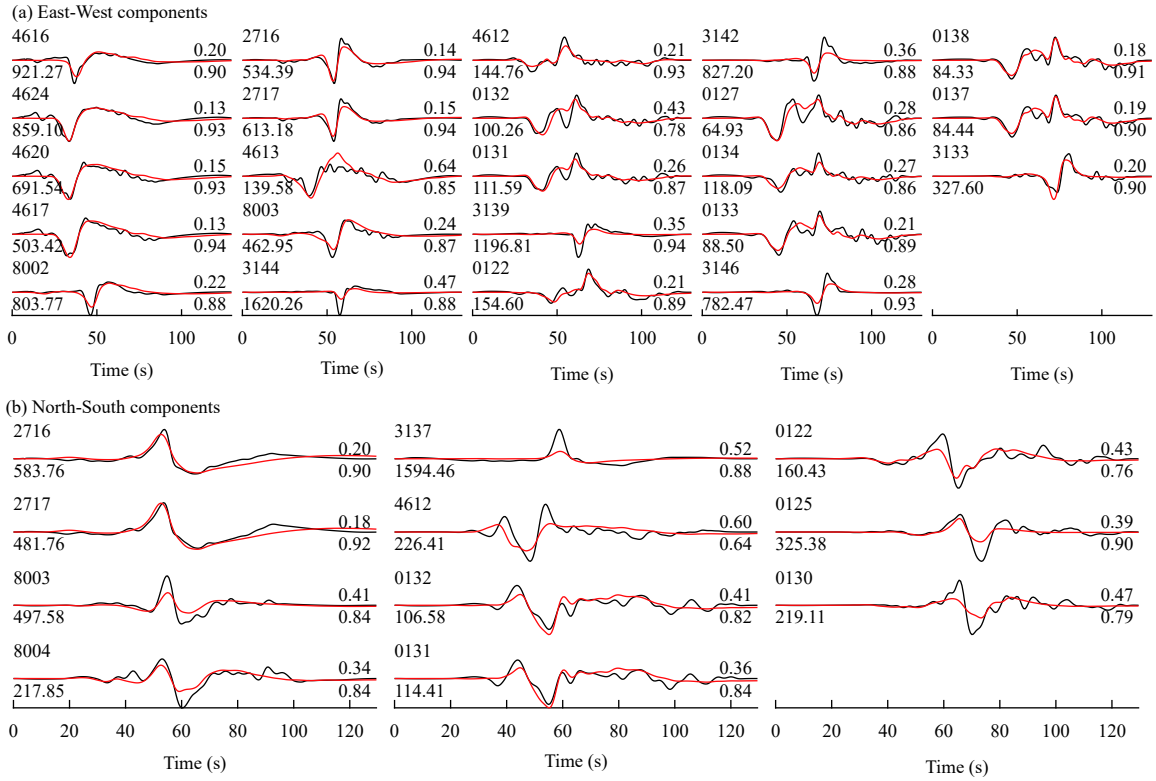

Figure S3. Strong-motion waveform fittings of the M_W7.8 earthquake based on single-fault model. The filtering frequency band is 0.01–0.2 Hz. For each component, the station code, maximum absolute value, normalized misfit and correlation coefficient are marked on the top left, bottom left, top right and bottom right, respectively. The normalized misfit of all components is 0.29.

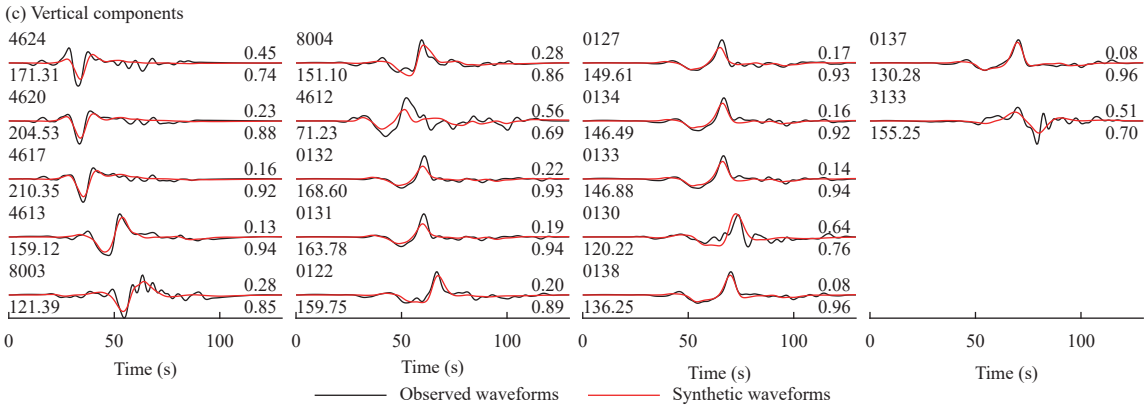

Figure S3. Continued.

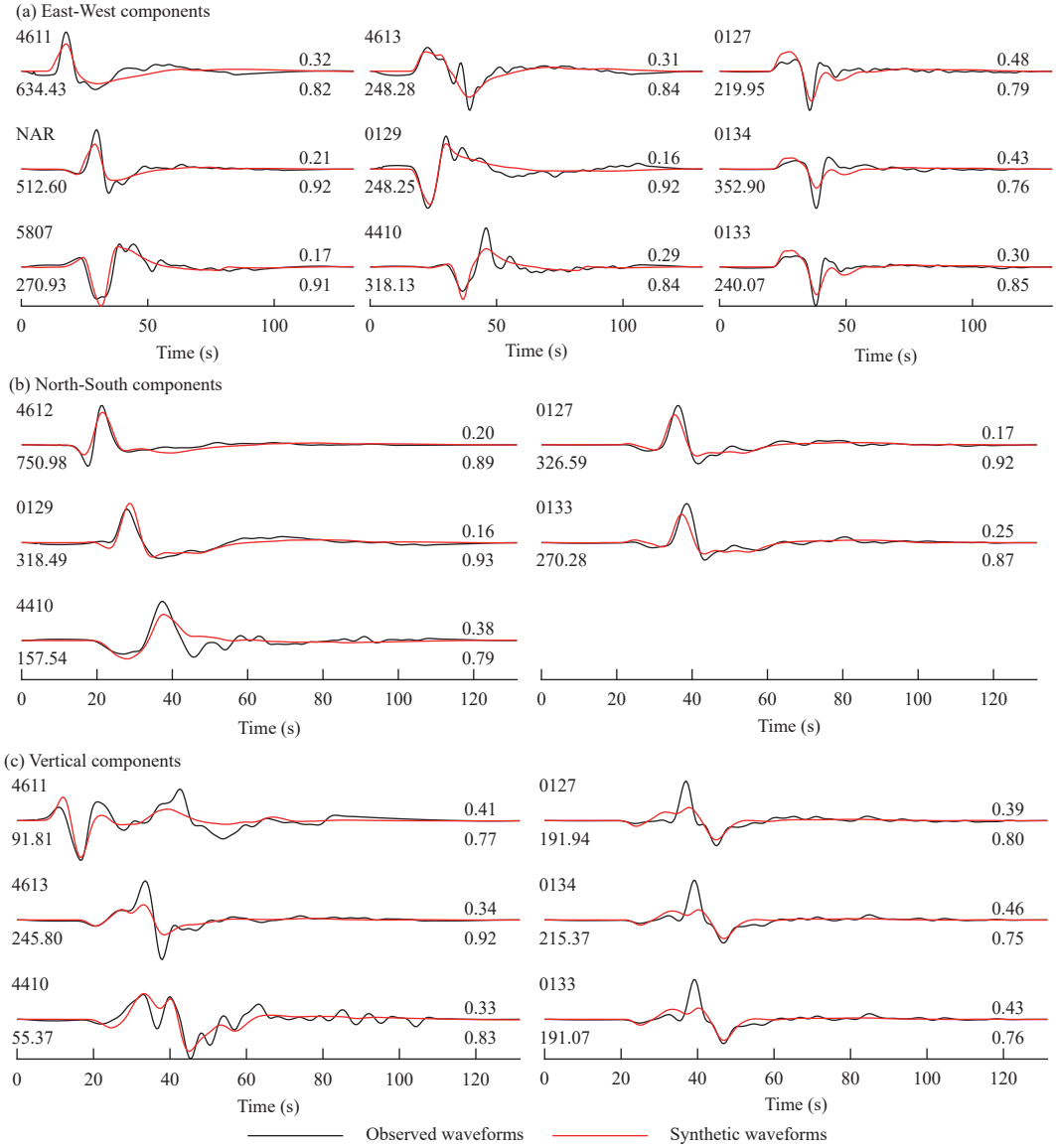

Figure S4. The same as Figure S3 but for the M_W7.6 earthquake inversion. The normalized misfit of all components is 0.34.

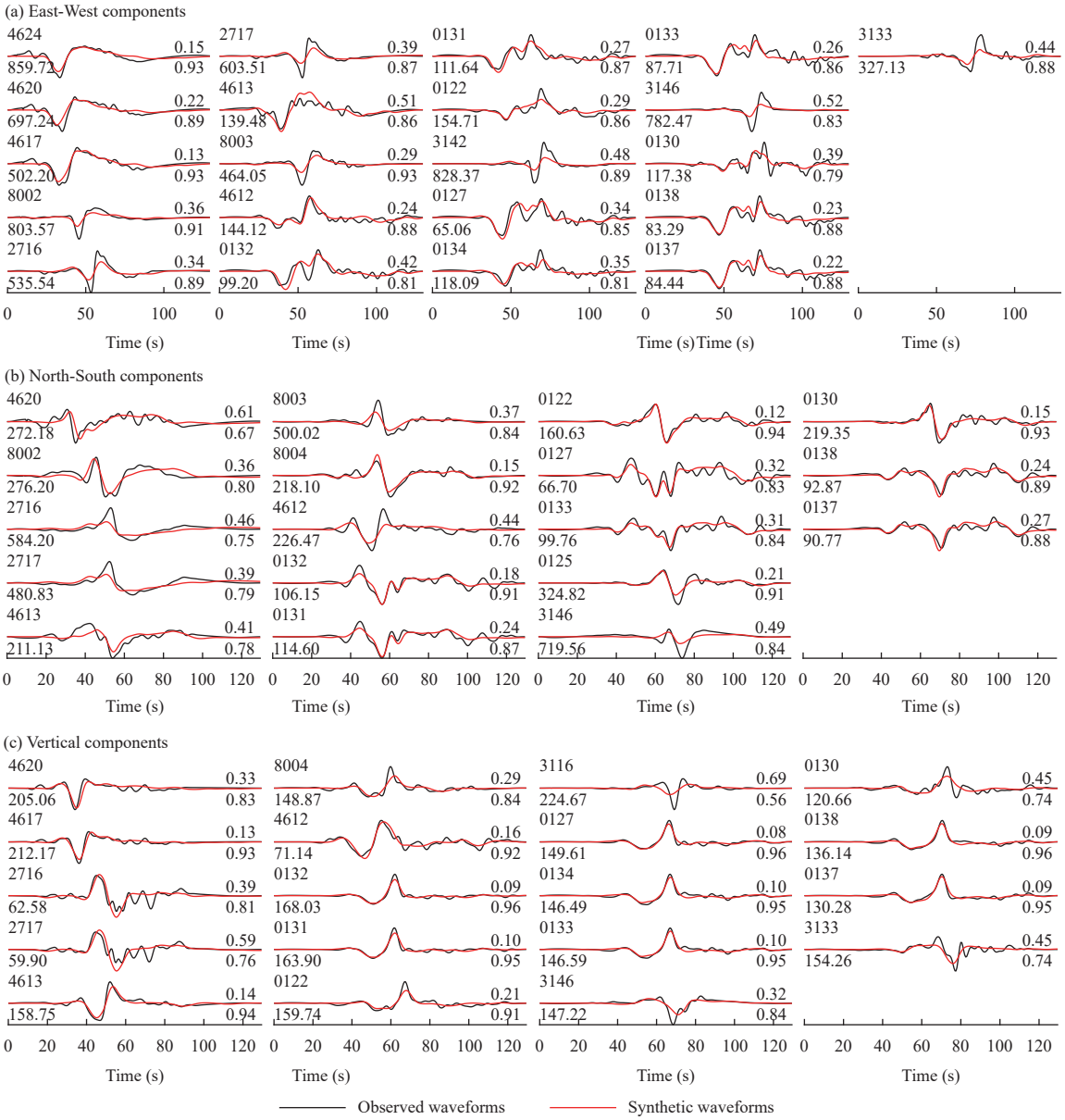

Figure S5. The same as Figure S3 but for the M_W7.8 earthquake with a two-segment fault model. The normalized misfit of all components is 0.30.

Table S1. The strong-motion stations used for inversions.

Station	Longitude (°E)	Latitude (°N)	Station	Longitude (°E)	Latitude (°N)
0122	35.8202	37.4339	3142	36.3661	36.4980
0125	35.7958	37.0152	3144	36.4857	36.7569
0127	35.9204	37.8162	3146	36.2270	36.4908
0129	36.2109	38.2592	4410	37.6790	38.8668
0130	35.6710	37.2519	4611	37.2843	37.7472
0131	36.1153	37.8566	4612	36.4819	38.0239
0132	36.1149	37.8559	4613	36.3574	37.5701
0133	35.8640	37.7455	4616	36.8384	37.3755
0134	35.8645	37.7443	4617	36.8303	37.5855

Continued

Station	Longitude (°E)	Latitude (°N)	Station	Longitude (°E)	Latitude (°N)
0137	35.7233	37.7049	4620	36.8984	37.5857
0138	35.7234	37.7049	4624	36.9177	37.5361
2716	36.6883	36.8564	5807	37.2475	38.7269
2717	36.6910	36.8555	8002	36.5620	37.1916
3133	36.5736	36.2432	8003	36.2694	37.0842
3137	36.4885	36.6929	8004	36.0976	37.3799
3139	36.4144	36.5838	NAR	37.1574	37.3919